3D Printing of Low-Filled Basalt PA12 and PP Filaments for Automotive Components

Journal of
Composites Science

MDPI

Article

3D Printing of Low-Filled Basalt PA12 and PP Filaments for Automotive Components

Federico Lupone [1], Jacopo Tirillò [2], Fabrizio Sarasini [2], Claudio Badini [1] and Claudia Sergi [2,*]

[1] Department of Applied Science and Technology, Politecnico di Torino, Corso Duca degli Abruzzi 24, 10129 Turin, Italy; federico.lupone@polito.it (F.L.); claudio.badini@polito.it (C.B.)
[2] Department of Chemical Engineering Materials Environment, Sapienza Università di Roma and UdR INSTM, Via Eudossiana 18, 00184 Rome, Italy; jacopo.tirillo@uniroma1.it (J.T.); fabrizio.sarasini@uniroma1.it (F.S.)
* Correspondence: claudia.sergi@uniroma1.it

Abstract: Fused Deposition Modeling (FDM) enables many advantages compared to traditional manufacturing techniques, but the lower mechanical performance due to the higher porosity still hinders its industrial spread in key sectors like the automotive industry. PP and PA12 filaments filled with low amounts of basalt fibers were produced in the present work to improve the poor mechanical properties inherited from the additive manufacturing technique. For both matrices, the introduction of 5 wt.% of basalt fibers allows us to achieve stiffness values comparable to injection molding ones without modifying the final weight of the manufactured components. The increased filament density compared with the neat polymers, upon the introduction of basalt fibers, is counterbalanced by the intrinsic porosity of the manufacturing technique. In particular, the final components are characterized by a 0.88 g/cm^3 density for PP and 1.01 g/cm^3 for PA12 basalt-filled composites, which are comparable to the 0.91 g/cm^3 and 1.01 g/cm^3, respectively, of the related neat matrix used in injection molding. Some efforts are still needed to fill the gap of 15–28% for PP and of 26.5% for PA12 in tensile strength compared to injection-molded counterparts, but the improvement of the fiber/matrix interface by fiber surface modification or coupling agent employment could be a feasible solution.

Keywords: 3D printing; FDM; basalt; polypropylene; polyamide 12

Citation: Lupone, F.; Tirillò, J.; Sarasini, F.; Badini, C.; Sergi, C. 3D Printing of Low-Filled Basalt PA12 and PP Filaments for Automotive Components. *J. Compos. Sci.* **2023**, *7*, 367. https://doi.org/10.3390/jcs7090367

Academic Editor: Francesco Tornabene

Received: 17 July 2023
Revised: 23 August 2023
Accepted: 26 August 2023
Published: 1 September 2023

1. Introduction

Additive manufacturing (AM) is an on the rise technique with a great potential in many industrial fields thanks to numerous advantages such as a higher freedom of design, waste minimization and fast prototyping [1–3]. Among these advantages, product customization assumes a great importance, enabling the ability to tailor product features as a function of consumer needs and wishes. This capability is fundamental in the biomedical, surgical and prosthetic industry sectors [4–9], who aim to improve the life quality of the patient, but can also be exploited to tailor consumer goods features depending on the requirements. This capability also allows for the promotion of a new commercial approach moving from the well-established Mass Production to the innovative Mass Customization which, in the framework of Industry 4.0, ensures product customization together with high production rates [10].

The higher freedom of design of AM enables and empowers the great potential of generative design (GD) and topology optimization (TO) to manufacture lighter and improved mechanically performing structures [11,12]. GD does not use an initial shape but, through an iterative process, searches for the optimal manner of growing the structure by applying a series of geometric and mechanical constraints. TO focuses on removing unnecessary material from the original shape following a series of constraints; thus, it creates designs with minimal mass and maximal stiffness [13]. These techniques can significantly improve

the performance in the automotive, aeronautical and aerospace sectors, ensuring the same mechanical performance with a lower weight [14,15], consequently promoting a reduction in the related fuel consumption.

Both product customization and structure lightweighting assume a key role in the automotive industry, making AM a valid and compelling alternative to traditional manufacturing techniques. Among the 3D printing techniques available, Fused Deposition Modeling (FDM) is designed for thermoplastic polymers and is the cheapest option, with machine investment costs from $2000 to $15,000 compared to the $18,500 to $100,000 of Selective Laser Sintering (SLS), according to the data reported by Formlabs [16]. FDM is also the cheapest one from the raw materials perspective, with costs around $50/kg compared with the $500/kg of SLS [17]. Despite all these advantages, it is well known that polymeric components produced by FDM are characterized by lower mechanical performance than the corresponding injection molding ones due to the high porosity generated by the discontinuities between adjacent layers [18,19].

On this basis, the present work proposes a viable way to exploit the advantages deriving from FDM—i.e., GD and TO, product customization and low investment costs—while trying to fix the main issue related to lower mechanical performance by using low-filled polymeric filaments. The two main polymeric materials used in the automotive sector are polypropylene (PP) and polyamides (PA) [20,21]. In particular, Grand View Research reported that PP led the automotive plastic market in 2021, accounting for more than 30% [22], with applications in dashboards, doors, pillar trims and seat carriers. Concerning PA, the automotive industry accounts for almost 40% of the global demand of this polymer family [23]. In light of this, PP and PA12 filaments reinforced with a 5 wt.% of short basalt fibers were considered in the present work.

Basalt is a mineral from volcanic rocks and is a bio-based alternative to glass fibers. It is characterized by comparable mechanical properties to E-glass fibers and by a greener manufacturing process, in which the energy consumption is lower and no addition of chemicals is required [24]. Many studies already assessed its effect on PLA 3D printing filaments [25,26], but no studies are available on PA12/basalt filament and only one paper by Ghabezi et al. [27] is available on PP/basalt filament where a recycled PP was considered. Recently Zhang and Sun [28] investigated the 3D printing of continuous basalt fibers (CBF) reinforced polyamide (PA), acrylonitrile butadiene styrene (ABS) and high impact polystyrene (HIPS) components. They showed that PA/CBF composites had the best ability to maintain material integrity under high stress. In light of this, PP and PA12 filaments reinforced with a 5 wt.% of short basalt fibers were produced in the present work to improve the mechanical performance of the 3D-printed components while preserving their lightness. After an initial thermal, i.e., by thermogravimetric analysis (TGA) and differential scanning calorimetry (DSC), as well as morphological characterization, the filaments were used to 3D print the final components, and the mechanical performance of the latter was characterized by tensile tests correlated with component microstructures by fracture surface analysis and density evaluation through pycnometry.

2. Materials and Methods

2.1. Materials

Two thermoplastic polymers widely used in the automotive industry were investigated in the present work, i.e., PP and PA12. Polypropylene pellets (Moplen PP567P) supplied by LyondellBasell (Rotterdam, The Netherlands) with a Melt Mass Flow Rate (230 °C/2.16 kg) of 8 g/10 min and a density of 0.9 g/cm^3 were used to produce the printing filament. The selected polypropylene is a homopolymer specifically designed for the production of continuous filaments. Concerning PA12, the microcrystalline transparent Trogamid CX7323 supplied by Evonik Industries AG (Essen, Germany) with a density of 1.02 g/cm^3, a Melt Volume Flow Rate (260 °C/2.16 kg) of 8.2 cm^3/10 min and a low water absorption compared to other polyamide grades that was suitable for injection molding and extrusion was selected. Chopped basalt fibers were supplied by Incotelogy GmbH (Pulheim, Germany)

with a nominal diameter of 13 µm and a nominal length of 3.2 mm. The fibers were coated by different commercial surface sizes to improve the compatibility with polypropylene and polyamide matrices.

2.2. Filaments Production

Both PP and PA12 printing filaments were produced with a 5 wt.% of basalt fibers content using the experimental set up reported in Figure 1. Polymer pellets and chopped fibers were mixed and homogenized with a Thermo Scientific Process 11 (Thermo Fisher Scientific, Waltham, MA, USA) co-rotating twin screw extruder to manufacture round-shaped filaments with a constant diameter around 1.75 mm.

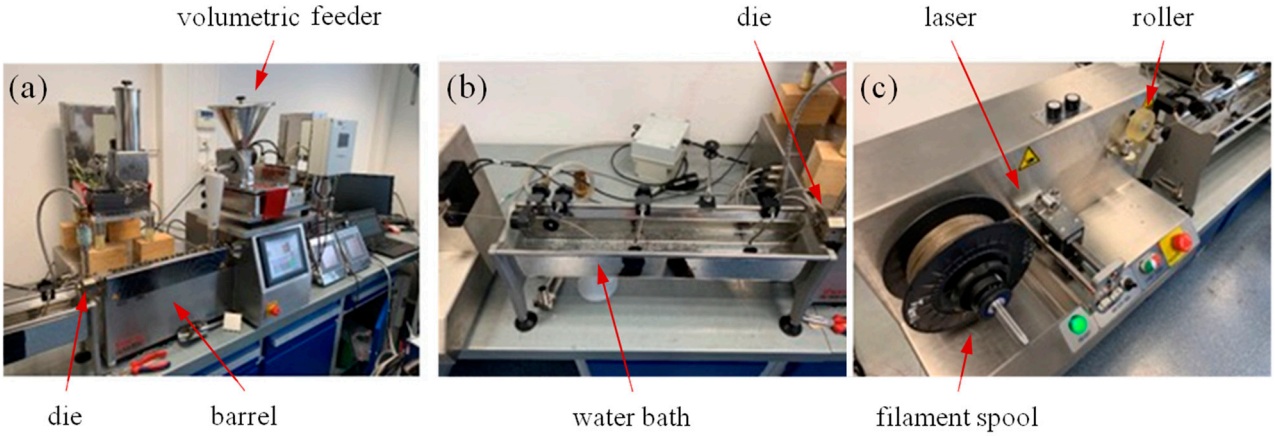

Figure 1. Experimental setup used for filament manufacturing: (**a**) twin-screw extruder with single-screw volumetric feeder, barrel and die, (**b**) cooling unit and (**c**) spooling unit with roller and laser measuring system for real-time monitoring of the filament diameter.

The extruder presents a barrel and a cylindrical die and was equipped with a single-screw volumetric feeder (Figure 1a). The barrel is composed of eight different heating zones, each of which is monitored with a thermocouple to precisely control the temperature profile in order to ensure proper compounding and processability of the composite materials. The process parameters used to extrude the different fiber-reinforced polymer filaments are summarized in Table 1.

Table 1. Process parameters used to produce the short fiber-reinforced polymer filaments: temperature profile of the extruder from the feeder to the die and rotation speed of the screw and puller.

Filament	Barrel Zone Temperatures (°C)								Screw Speed	Puller Speed
	T_1	T_2	T_3	T_4	T_5	T_6	T_7	die	(rpm)	(rpm)
PP-Basalt	170	190	190	190	190	190	190	180	150	4
PA12-Basalt	250	280	280	280	280	280	260	260	150	4

Downstream of the die exit, the filament was homogeneously cooled in a water bath (Figure 1b) and pulled down by a roller positioned along the extrusion line, whose rotation speed can be regulated to reach the desired diameter (Figure 1c). The subsequent spooling unit is automatic and was equipped with a laser measuring system to enable the real-time monitoring of the filament diameter (Figure 1c). This control is crucial because the FDM technique requires filaments with a diameter of 1.75 mm and close dimensional tolerances (±0.05 mm) because higher deviations would result in processing issues such as nozzle obstruction or intermittent extrusion.

2.3. Specimens 3D Printing

PP and PA12 basalt-filled filaments were printed by Fused Deposition Modeling (FDM) using Roboze One printer (Roboze SpA, Bari, Italy), i.e., a professional desktop FDM printer with a build envelope of 280 × 220 × 300 mm^3 and a heated build platform. The printer was equipped with a steel extruder nozzle with a 0.6 mm diameter in place of the standard brass one to prevent nozzle damage due to fiber abrasiveness.

For each material, dog-bone shaped samples and rectangular plates were fabricated using a single perimeter contour and a ±45° printing strategy for the infill region, i.e., the orientation of the extruded beads is alternated between 45° and −45° in each layer. This printing layup is one of the most common patterns to produce polymeric parts by FDM because it ensures high mechanical properties while maintaining a high degree of in-plane isotropy. All samples were printed in the flatwise direction and the infill density was set equal to 100% to maximize the mechanical performances of the final parts. The dimensions of tensile samples were selected according to the ISO 527-2:2012 standard (type 1BA test specimens) to evaluate the tensile properties of the composites, while the rectangular plates (35 × 35 × 3 mm^3) were used for microstructural analysis and density measurements. For polyamide-based composites, the adhesion with the build platform was ensured by a three-layer raft printed just below the first layer of the samples; for the PP-Basalt filament, it was necessary to apply an adhesive plate with a rough surface made of polypropylene itself onto the build platform due to the low adhesion of PP with the standard build platforms.

The 3D printing parameters used are summarized in Table 2 for each formulation, and they were optimized through empirical printing trials on the basis of the thermal properties of the filaments. The extrusion temperature was set a few degrees above polymer melting to promote the formation of beads with stable geometry while preventing material degradation. The build platform temperature was set just above the glass transition to avoid undesired part distortion. Simplify3D software was used to set the process parameters into the g-code file.

Table 2. 3D printing parameters used to manufacture PP and PA12 basalt-filled samples for tensile and microstructural characterization using Roboze One FDM printer.

Process Parameters	PP-Basalt	PA12-Basalt
Extrusion temperature (°C)	260	300
Build platform temperature (°C)	50	70
Extrusion speed (mm/min)	50	50
Layer thickness (mm)	200	200
Build platform/extruder gap (μm)	250	200

2.4. Physical and Morphological Characterization

X-ray diffraction (XRD) was employed to investigate the crystalline structure of the polymer matrices of the raw filaments using a Panalytical PW3040/60 X'Pert PRO diffractometer (Malvern Panalytical, Malvern, Worcestershire, UK) equipped with a standard Cu-Kα X-ray source. All diffraction patterns were obtained using a step size of 0.013° in the 2θ interval between 10° and 60°.

The density of both raw filaments and 3D-printed samples was measured through a Ultrapyc 5000 gas pycnometer (Anton Paar QuantaTec, Boynton Beach, FL, USA). Concerning the filament, pieces with a total mass of 1 ± 0.2 g were tested, while six rectangular 3D-printed coupons (10 × 10 × 3 mm^3) were tested for each filament type. The latter were extracted from the printed plate through high precision cutting using the Brilliant 220 cut-off machine (QATM Gmbh, Mammelzen, Germany). All measurements were performed according to the ISO 1183-3 standard with helium as probing gas. The void content (φ) of the printed specimens was calculated using Equation (1):

$$\varphi(\%) = \frac{\rho_f - \rho_{ps}}{\rho_f} * 100 \quad (1)$$

where ρ_f and ρ_{ps} are the density of the raw filaments and of the 3D-printed samples, respectively.

The fiber length distribution of the basalt-filled composites from both filament and 3D-printed samples was evaluated by dissolving the PP and PA12 matrices in tetrachloroethylene at 120 °C and formic acid at 100 °C, respectively. The suspended fibers were placed on a glass plate and their length was determined using the optical microscope Nikon Eclipse 150L (Nikon, Tokyo, Japan), and at least 500 fiber lengths were recorded for each sample.

2.5. Thermal Characterization

Differential Scanning Calorimetry (DSC) was used to investigate the thermal behavior and the crystalline fraction of the filaments. Samples were tested with a DSC 214 Polyma (Netzsch, Selb, Bayern, Germany) in a nitrogen atmosphere using a standard heating/cooling rate of 10 °C/min. The heating/cooling ramps used for the calorimetric tests were from 30 to 220 °C for PP/BAS filament and from 30 to 300 °C for PA12/BAS filament. Characteristic temperatures, i.e., melting, crystallization and glass transition temperature, as well as melting enthalpy, were calculated from the DSC curves, and the crystalline fraction (Xc) of the polymer matrices was obtained by applying Equation (2):

$$X_c(\%) = \frac{\Delta H_m}{\Delta H_{m0}\,(1 - w_f)} * 100 \quad (2)$$

where ΔH_m is the melting enthalpy experimentally measured, ΔH_{m0} is the melting enthalpy of the fully crystalline polymer matrix and w_f is fibers weight fraction. The values ΔH_{m0} used are 207 J/g for PP and 245 J/g for PA12 [29].

Thermogravimetric analysis (TGA) was used to evaluate the thermal stability and fiber content of the filaments. Specimens were placed in alumina crucibles and heated from 25 °C to 800 °C with a heating rate of 10 °C/min in an inert nitrogen atmosphere. A TG209 F1 Libra (Netzsch, Selb, Bayern, Germany) was used to perform all experiments.

2.6. Mechanical Characterization

Tensile tests were performed on the 3D-printed samples using an MTS Criterion Model 43 universal testing machine (MTS Systems Corporation, Eden Prairie, MN, USA). Tests were carried out at room temperature according to the ISO 527-2 standard using a crosshead speed of 1 mm/min, a load cell of 5 kN and an extensometer with a 25 mm gauge length. For each material, at least four samples were tested. Before tensile testing, PA12 composite samples were dried at 80 °C for 6 h to remove moisture.

The fractured surfaces of the printed samples after tensile testing were analyzed using a Phenom ProX desktop scanning electron microscope (SEM) (Thermo Fisher Scientific, Waltham, MA, USA) to study the microstructure of the composites, the fiber/matrix interfacial adhesion and the failure mechanism. The micrographs were collected at an accelerating beam voltage of 5 kV and a thin platinum layer was deposited on the samples by sputter coating before analysis to prevent electrostatic charging.

3. Results and Discussion

3.1. Filament Characterization

The first step in filament characterization was focused on the evaluation of their dimensional accuracy by means of a digital vernier caliper measuring the diameter in different points along their length. The target diameter was 1.75 mm and the industrial gold standard for filament diameter tolerance is ±0.05mm even if a deviation of ±0.1 mm is also considered acceptable [30]. The dimensional accuracy of the PA12 filament was quite good with an average diameter of 1.73 mm and a tolerance of ±0.03 mm, which can be suitably included in the gold standard tolerances. The PP filament displayed a lower accuracy with an average diameter of 1.64 mm and a tolerance of ±0.03 mm, which makes it almost fall in the acceptable range in any case.

The thermal stability of the filaments was investigated by TGA and the related mass loss and derivative curves are reported in Figure 2. PP filament displays a single degradation step coherently with the radical random scission typical of polyolefins [31], and it occurs between 400 and 480 °C with a maximum degradation temperature of 459 °C evaluated at the minimum point of the DTG curve. These results are coherent with the ones by Esmizadeh et al. [31], who reported a maximum degradation temperature at around 440 °C. The PA12 filament was characterized by a two-step degradation with a first mass loss of 1.6% at 149 °C and a second mass loss between 425 and 490 °C with a maximum degradation temperature at 469 °C. The first mass drop is analogous to the one observed by Touris et al. [32] and it must be ascribed to moisture removal due to the intrinsic hygroscopicity of polyamides [33], while the second mass loss is coherent with the one reported by Jose et al. [34] at around 463 °C. PP filament displays a residual mass of 4.4 ± 0.3%; PA12 filament displays a 4.8 ± 0.4% residual mass. These values are both compatible with the 5 wt.% of basalt fiber added during the compounding process, further proving the good control of the extrusion process.

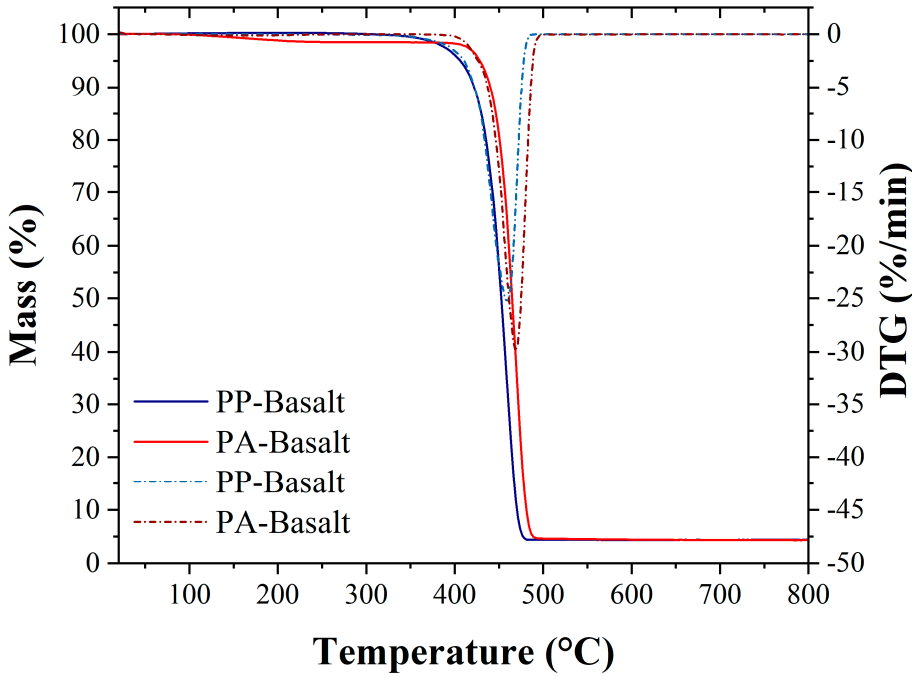

Figure 2. TGA and DTG curves of PP and PA12 basalt-filled filaments.

DSC allowed us to take the filaments' thermal characterization a step further, and the related curves are shown in Figure 3; the main resulting parameters are summarized in Table 3. Indeed, the 3D printing extrusion temperatures were selected to work well above polymers' melting temperature to ensure a good fluidity of the printed filaments to improve layer adhesion.

Interesting results can be also observed in terms of polymer crystallinity. PP is characterized by a 36.8% degree of crystallinity, which must be ascribed to the monoclinic α structure that is the most thermodynamically stable [35], as also confirmed by the XRD spectrum shown in Figure 4. Indeed, the peaks observed at 14°, 16.8°, 18.4°, 20.9°, 21.7°, 25.4°, 28.3° and 42.5° are related to the monoclinic α crystalline planes (110), (040), (130), (111), (041), (060) along with (150), (220) and (212) [36] (JCPDS card no. 66-1214), respectively.

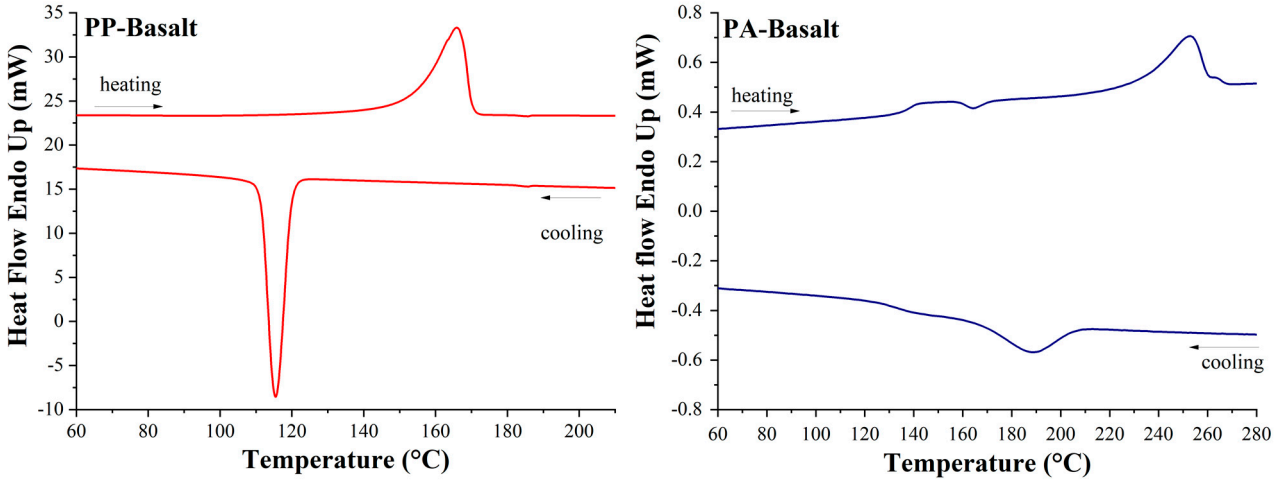

Figure 3. DSC curves of PP and PA12 basalt-filled filaments.

Table 3. Glass transition, crystallization and melting temperatures and crystallinity degree of PP and PA12 basalt-filled filaments.

Sample	Glass Transition Temperature (°C)	Melting Temperature (°C)	Crystallization Temperature (°C)	Degree of Crystallinity (%)
PP-Basalt_filament	-	166	115	36.8
PA12-Basalt_filament	139	252	191	8.7

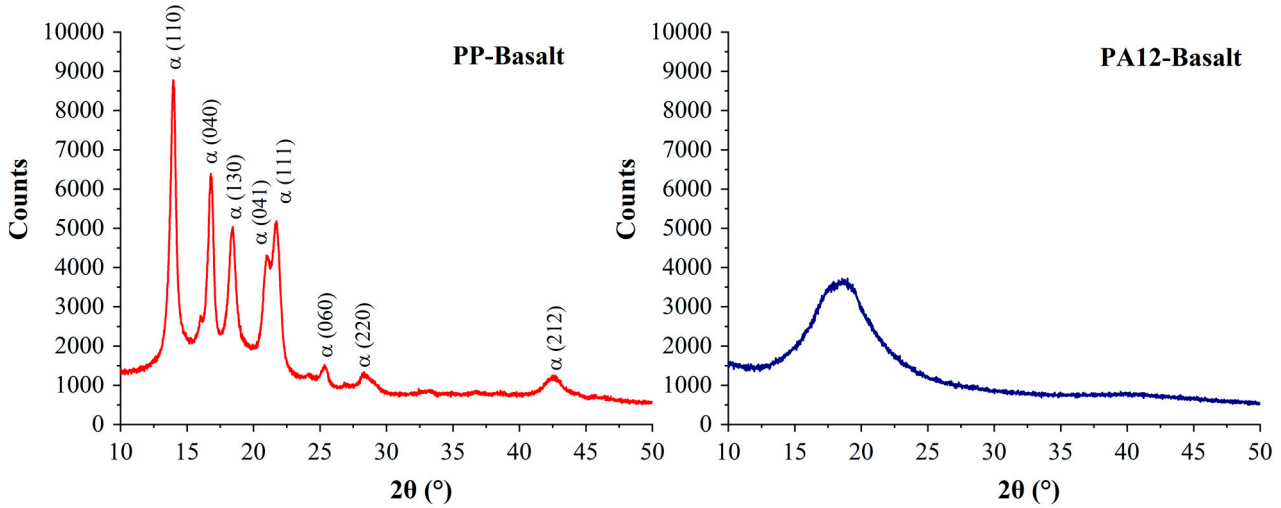

Figure 4. XRD spectra of PP and PA12 basalt-filled polymers.

On the contrary, PA12 Trogamid CX7323 is characterized by a very low degree of crystallinity, i.e., 8.7%; therefore, an amorphous response with a single broad peak is observed when analyzed by XRD. This can be explained considering that it is a microcrystalline polymer where the crystallites are pretty small and do not scatter visible light, making the material transparent. This peculiar structure allows us to explain why the 18.5° broad peak observed in the XRD spectrum of the present work is not compatible with the typical PA12 crystalline structures, which can be either monoclinic (α) or hexagonal (γ) structures depending on the manufacturing process. In particular, the α structure would display a diffraction peak at 20.2° deriving from the (200) plane and a diffraction peak at 23.1° deriving from the (010) plane; the γ structure would display a diffraction peak at 22.5° deriving from the (001) plane [37]. This unique microstructure is well reflected in the DSC curve of the PA12-basalt filled filament, where a clear glass transition at 139 °C and a

broad and shallow melting peak at 252 °C can be observed. Although these temperatures are higher compared to standard polyamide 12, the values agree well with the technical data sheet of the polymer matrix used in this study, i.e., Trogamid CX7323, where a glass transition and melting temperature of 140 °C and 250 °C are reported, respectively. It is also worth noting that, in addition to the main melting peak, a smaller one can be observed, which might be ascribed to a distribution of crystal phases [38].

Finally, both PP and PA12 fiber length distribution was evaluated, and the resulting data are reported in Figure 5. Despite using the same type of basalt fibers, the same screw speed and profile as well as a compounding temperature 30 °C higher than the corresponding melting temperature for both PP and PA12, the latter displays a fiber length distribution with a lower average length, i.e., 337 µm against 393 µm, and is characterized by a narrower width, i.e., 123 µm against 197 µm. This highlights a higher degradation of the fibers during the compounding phase with a significant disappearance of the longest fibers and can be likely ascribed to the different nature of the polymeric matrices. Polypropylene is intrinsically nonpolar, whereas polyamides are characterized by a certain polarity that results in a stronger interaction between the amide groups of a macromolecule and the carboxylic acid group of the adjacent ones [39]. Being equal the overheating applied while compounding, the stronger interaction of PA12 macromolecules may result in a higher viscosity of the melt, which increases the bending moment exerted on the fibers and determines a higher reduction in their length.

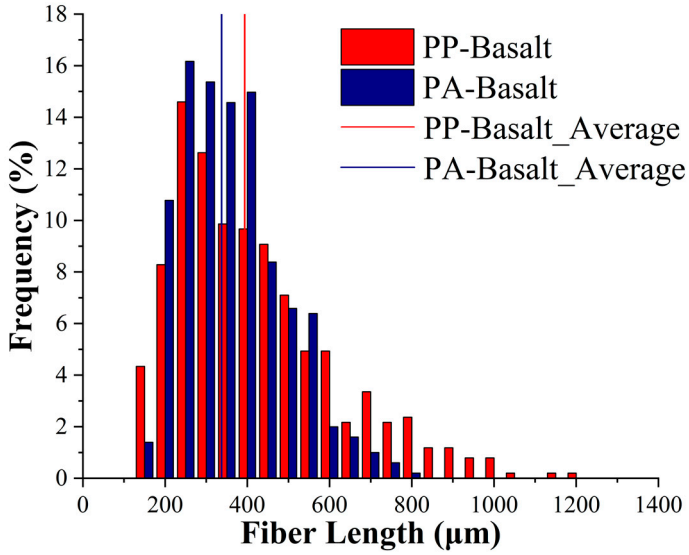

Figure 5. PP and PA12 basalt-filled filaments fiber length distribution.

3.2. 3D-Printed Specimens' Characterization

3.2.1. Physical and Microstructural Characterization: Density Measurement and Fiber Length Distribution

The main weakness of FDM is the higher porosity of the resulting components compared to the ones obtained by injection molding. The latter is mainly caused by an incomplete coalescence of adjacent extruded filaments, which results in a poorer adhesion and consequently in lower mechanical properties. Therefore, the porosity of the 3D-printed specimens was evaluated by comparing the density of the raw filaments with the density of the specimens by helium pycnometry. PP filament displays a density of 0.94 g/cm^3, whereas the 3D-printed specimen displays a 0.88 g/cm^3 density with 6.3% porosity. PA12 filament displays a density of 1.06 g/cm^3, whereas the 3D-printed specimen displays a 1.01 g/cm^3 density with 4.3% porosity. The increase in porosity resulting from 3D printing is also confirmed by the optical micrographs reported in Figure 6. The higher porosity of PP specimens can likely be ascribed to the higher crystallinity of this matrix compared to PA12. This implies a sudden increase of viscosity once the extruded filament undergoes

cooling which, in turn, hampers full coalescence between adjacent filaments and successive layers.

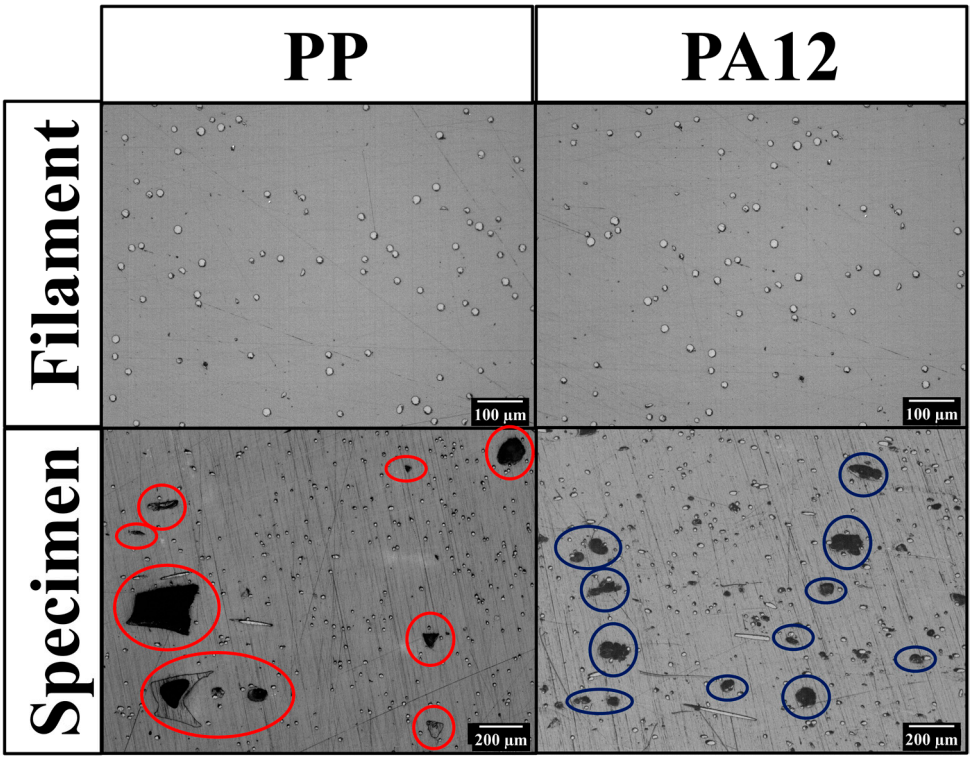

Figure 6. PP and PA12 micrographs of the neat filaments and of the 3D-printed specimens. Red and blue circles highlight porosity in the samples.

Considering the strong influence of fiber length in the composite mechanical response, the fiber length distribution of both polymeric configurations was also evaluated after the specimens' 3D printing, and the resulting data are shown in Figure 7. PP specimens display just a slight decrease of 16 µm in the average fiber length, resulting from the disappearance of the longest fibers belonging to the 1050–1200 µm range. This can be likely ascribed to the reduced dimension of the extruding nozzle, i.e., 0.6 mm, which hinders the passage of longer fibers unless perfectly aligned along the printing direction.

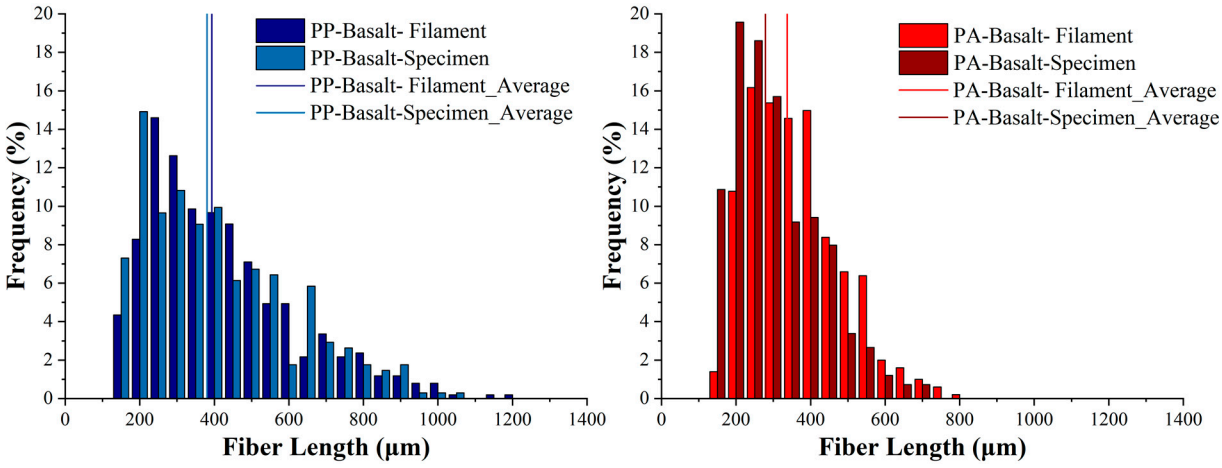

Figure 7. Comparison of the fiber length distributions between 3D printing filament and 3D-printed specimens for both PP and PA12 matrices.

The situation for PA12 is different, where a further reduction of 60 µm in fibers' average length and a further narrowing of the distribution, i.e., 117 µm against 123 µm, were observed. This difference in behavior can be likely ascribed to polymer rheology. In particular, PP filament was 3D printed using 260 °C, which is 100 °C higher than the polymer melting temperature; thus, a good fluidity of the melt is ensured. On the contrary, PA12 was 3D printed using 300 °C as the extrusion temperature, which is the upper limit of the 3D printer, providing only 50 °C overheating, which entails a higher viscosity of the melt and an increase in the bending moments applied on the fibers. Moreover, polycondensation polymers, such as polyamides and polyesters, can experience an increase in viscosity over time as a consequence of post-condensation/thermo-degradative phenomena. Post-condensation phenomena are likely to occur if the moisture content of the polymer is less than that of the thermodynamic equilibrium, leading to an increase in the molecular weight of the polymer; however, this mechanism is predominant only if polymer melting takes place in an inert environment [40]. Conversely, chain scissions and cross-linking are more likely to occur when working in air, consequently leading to the extension of cross-linked fractions and to macromolecules branching, which hinders the macroscopic flows [41,42].

3.2.2. Tensile Properties

Finally, the mechanical performance of the two 3D-printed configurations under study was evaluated by tensile tests. The resulting properties are summarized in Table 4 for PP and Table 5 for PA12 and are compared with some results from literature. In both tables, the literature data need to be considered only as a benchmark, as there are many factors affecting the final mechanical properties (grade of polymer, molecular weight, final crystallinity degree, porosity and so forth). Concerning PP, the introduction of low contents of basalt fibers is quite promising in terms of tensile property enhancement, ensuring a strong improvement in tensile stiffness and strength. In particular, increases in tensile stiffness of 1695%, 458%, 382% and 25.7% were observed in the works proposed by Sodeifian et al. [43], Milosevic et al. [44], Milovanovic et al. [45] and Carneiro et al. [46], respectively. The results in terms of stiffness also compare well with the ones reported by Jin et al. [47], who used a 0° printing direction for the infill, which is perfectly parallel to the tensile test direction and consequently less critical.

Table 4. Comparison of the tensile properties of the PP-basalt filled configuration produced in the present work with those reported in previous works for 3D-printed PP and injection-molded PP.

Reference	Tensile Modulus [MPa]	Tensile Strength [MPa]
Present Work	1257.3 ± 307.2	23.1 ± 2.6
FDM Neat PP		
Sodeifian et al. [43]	≈70	≈20
Milosevic et al. [44]	≈225	≈16
Milovanovic et al. [45]	260.7	11.57
Carneiro et al. [46]	≈1000	≈27.5
Jin et al. [0° orientation] [47]	1267	16.7
Injection Molding Neat PP		
Sergi et al. [48]	1200	27.2
Karmaker et al. [49]	1230	27.8
Farotti et al. [50]	1253	32.1

The results are interesting even when compared with more traditional manufacturing techniques such as injection molding. In particular, the introduction of a low weight fraction of basalt fibers can help obtain the same stiffness achievable by injection molding and a tensile strength only 15–28% lower. This gap in tensile strength could be likely overcome by improving basalt fibers/matrix interface. Observing the fracture surface of the 3D-printed PP specimens reported in Figure 8, it can be noticed that some regions are able to ensure quite a satisfying interfacial adhesion between the matrix and the reinforcement (blue

arrows in Figure 8A). By contrast, in some other regions (Figure 8B), the fiber/matrix interface is quite poor (red arrows) and the fibers are characterized by a smooth surface that highlights a poor load transfer from the matrix. This must be ascribed to the hydrophobic nature of the PP matrix, which counteracts the -OH groups on the basalt fibers' surface [51]. In this perspective, the introduction of a coupling agent such as maleic anhydride-grafted polypropylene [52] or the modification of basalt fiber surfaces with silanes [53] would improve fiber/matrix interface and the resulting load transfer with an enhancement in tensile strength.

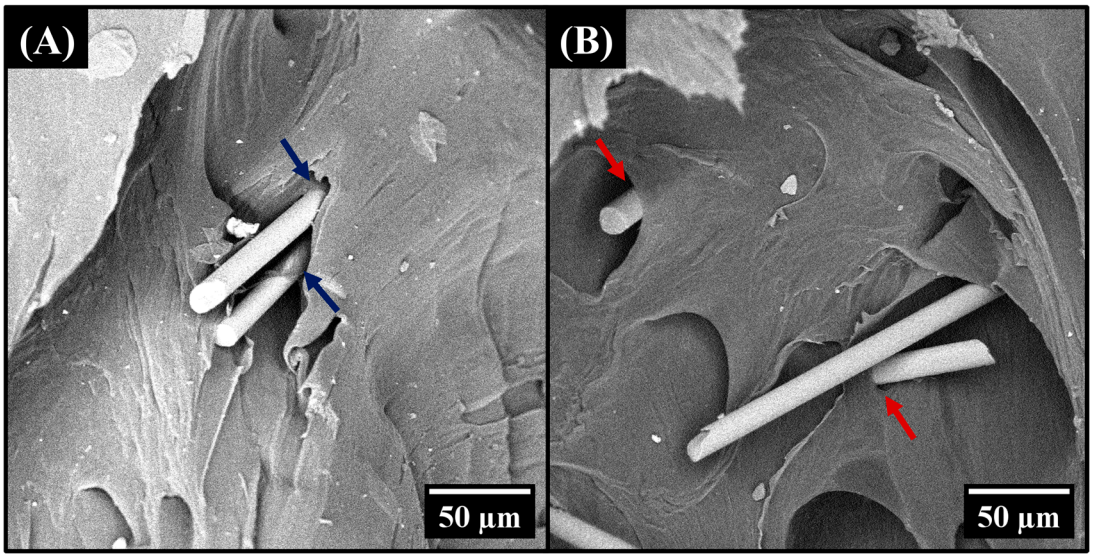

Figure 8. SEM micrographs of the fracture surface of PP basalt-filled, 3D-printed specimens. Satisfying interfacial adhesion (**A**) and poor interfacial adhesion (**B**) between the matrix and the reinforcement.

Even for PA12, the introduction of low contents of basalt fibers proved to be promising in improving the tensile properties of the 3D-printed component. In particular, increases in tensile stiffness of 245% and 59% were observed in the works proposed by Ferreira et al. [54] and by Liao et al. [55], respectively. Moreover, increases of 44.7% and 16.3% in tensile strength were compared to the works proposed by Ferreira et al. [54] and by Feng et al. [56], respectively. The tensile strength achieved is slightly lower, i.e., 8%, than the one obtained by Liao et al. [55], because even in this case, a 0° printing direction for the infill was selected. The results are also promising when compared with those reported for more traditional manufacturing techniques such as injection and compression molding. In particular, the introduction of basalt fibers ensures an increase of 29.7% in stiffness compared to injection molding and of 42.5% compared to compression molding. Some efforts are needed to reach the same tensile strength achievable with injection molding, which is still 26.5% higher.

Even in this case, the improvement of the fiber/matrix interface by coupling agent or fiber surface modification could be a suitable way to fill this gap in tensile strength. Indeed, as already observed for PP filaments, regions with a good interfacial adhesion (Figure 9A) are interspersed with regions of incompatibility between the fibrous reinforcement and the polymeric matrix (Figure 9B). Another possible solution could be the increase in filament manufacturing and 3D printing temperatures to reduce polymer viscosity and the resulting fiber length reduction, which is much more pronounced for PA12 compared to PP. Figure 10 shows one of the basalt fibers of the PA12 specimens. It is characterized by such a short length that it probably acts as a stress intensifier rather than a reinforcement.

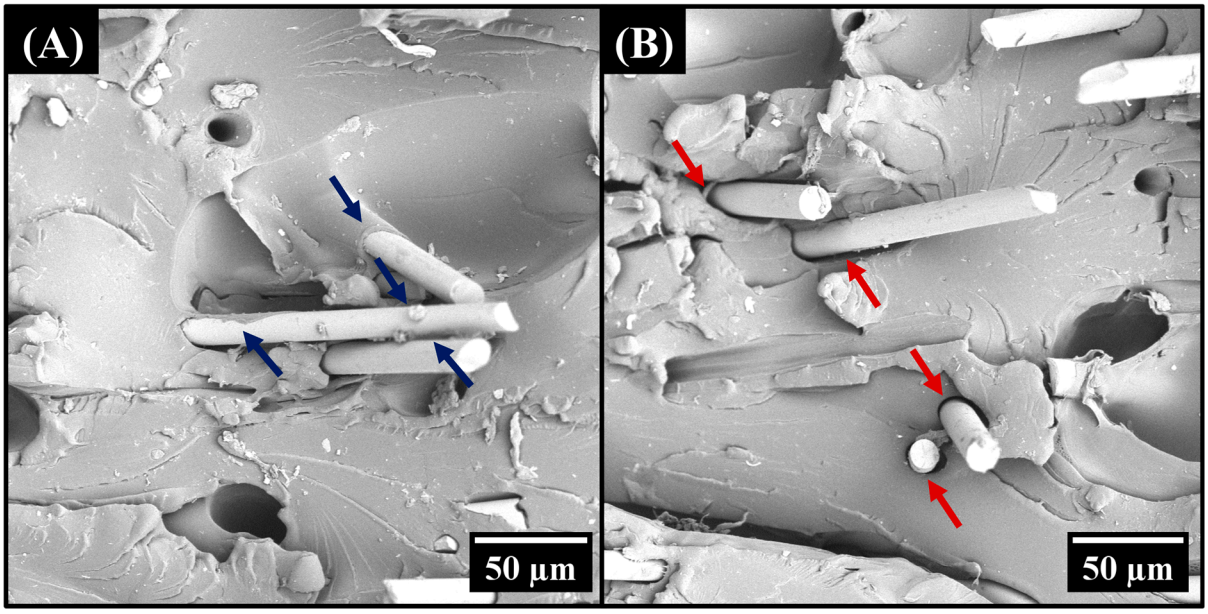

Figure 9. SEM micrographs of the fracture surface of PA12 basalt-filled, 3D-printed specimens. Satisfying interfacial adhesion (**A**) and poor interfacial adhesion (**B**) between the matrix and the reinforcement.

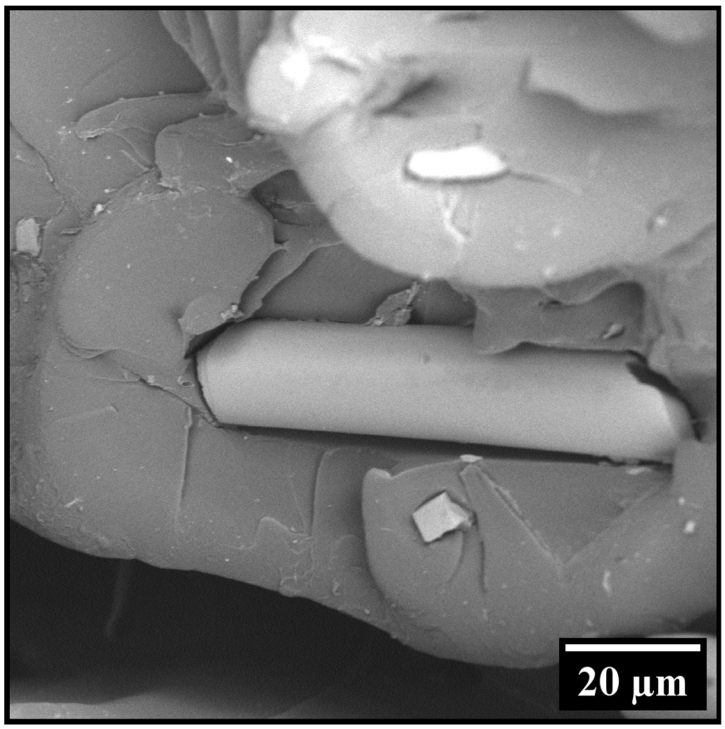

Figure 10. SEM micrograph of the fracture surface of PA12 basalt-filled, 3D-printed specimens.

Table 5. Comparison of the tensile properties of the PA12 basalt-filled configuration produced in the present work with those reported in previous works for 3D-printed, injection-molded and compression-molded PA12.

	Tensile Modulus [MPa]	Tensile Strength [MPa]
Present Work	1556.5 ± 41.3	42.7 ± 3.6
FDM Neat PA12		
Ferreira et al. [54]	451	29.5
Feng et al. [56]	-	36.7
Liao et al. [0° orientation] [55]	978.8	46.4
Injection Molding Neat PA12		
Meyer et al. [57]	1092	54
Compression Molding Neat PA12		
Nicharat et al. [58]	1200	40

4. Conclusions

3D printing is an effective technique that presents many advantages compared to traditional manufacturing processes, enabling generative design, topological optimization, and product customization. Considering FDM, it is also characterized by low investment costs. However, despite all these appealing features, the lower mechanical performance compared to injection molding and other manufacturing techniques deriving from the higher porosity of the final components is still a limit for the widespread use of this technique in industrial sectors such as the automotive one. On this basis, the present work proposes a viable way to exploit the advantages of FDM while trying to fix the main issue connected with the lower mechanical performance by exploiting low-filled polymeric filaments and focusing on PP and PA12 polymers, which are the most widely used in the automotive sector.

The tensile tests highlighted that for both PP and PA12, the introduction of a 5 wt.% of basalt fibers helped obtain stiffness values comparable to those obtained by injection molding without altering the final weight of the manufactured components. Indeed, the introduction of basalt fibers causes an increase in filament density compared to the neat polymers, i.e., 0.94 g/cm^3 in place of 0.91 g/cm^3 for PP and 1.06 g/cm^3 in place of 1.01 g/cm^3 for PA12, which is counterbalanced by the intrinsic porosity deriving from the manufacturing technique, leading to final components of 0.88 g/cm^3 for PP and 1.01 g/cm^3 for PA12.

Some efforts are still required to fill the gap of 15–28% and of 26.5% in tensile strength for both PP and PA12 compared to injection-molded samples, respectively. In particular, a modification of the matrix with coupling agents or a modification of basalt fibers' surface could be suitable ways to improve the fiber/matrix interface and the related load transfer to reach the mechanical performance of injection-molded parts.

Author Contributions: Conceptualization, J.T., F.S. and C.B.; methodology, F.L. and C.S.; validation, J.T., F.S. and C.B.; formal analysis, F.L. and C.S.; investigation, F.L. and C.S.; writing—original draft preparation, C.S.; writing—review and editing, F.L., J.T., F.S. and C.B.; visualization, C.S.; supervision, J.T., F.S. and C.B.; funding acquisition, J.T., F.S. and C.B. All authors have read and agreed to the published version of the manuscript.

Funding: This work has been supported by the Research Project AMICO (code ARS01_00758) funded by the Italian Ministry of Education, University and Research.

Data Availability Statement: All data are contained within the article.

Conflicts of Interest: The authors declare no conflict of interest.

References

1. Ngo, T.D.; Kashani, A.; Imbalzano, G.; Nguyen, K.T.Q.; Hui, D. Additive Manufacturing (3D Printing): A Review of Materials, Methods, Applications and Challenges. *Compos. Part B* **2018**, *143*, 172–196. [CrossRef]
2. Abdulhameed, O.; Al-ahmari, A.; Ameen, W.; Mian, S.H. Additive Manufacturing: Challenges, Trends, and Applications. *Adv. Mech. Eng.* **2019**, *11*, 1–27. [CrossRef]
3. Mahmood, A.; Akram, T.; Chen, H.; Chen, S. On the Evolution of Additive Manufacturing (3D/4D Printing) Technologies: Materials, Applications, and Challenges. *Polymers* **2022**, *14*, 4698. [CrossRef] [PubMed]
4. Lv, Y.; Wang, B.; Liu, G.; Tang, Y.; Lu, E.; Xie, K.; Lan, C.; Liu, J.; Qin, Z.; Wang, L. Metal Material, Properties and Design Methods of Porous Biomedical Scaffolds for Additive Manufacturing: A Review. *Front. Bioeng. Biotechnol.* **2021**, *9*, 641130. [CrossRef]
5. Singh, G.; Saini, A. Application of 3D Printing Technology in the Development of Biomedical Implants: A Review. *Trends Biomater. Artif. Organs* **2021**, *35*, 95–103.
6. da Silva, L.R.R.; Sales, W.F.; Campos, F.d.A.R.; de Sousa, J.A.G.; Davis, R.; Singh, A.; Coelho, R.T.; Borgohain, B. A Comprehensive Review on Additive Manufacturing of Medical Devices. *Prog. Addit. Manuf.* **2021**, *6*, 517–553. [CrossRef]
7. Parandoush, P.; Lin, D. A Review on Additive Manufacturing of Polymer-Fiber Composites. *Compos. Struct.* **2017**, *182*, 36–53. [CrossRef]
8. Yuan, S.; Li, S.; Zhu, J.; Tang, Y. Additive Manufacturing of Polymeric Composites from Material Processing to Structural Design. *Compos. Part B Eng.* **2021**, *219*, 108903. [CrossRef]
9. Fan, J.; Zhang, L.; Wei, S.; Zhang, Z.; Choi, S.K.; Song, B.; Shi, Y. A Review of Additive Manufacturing of Metamaterials and Developing Trends. *Mater. Today* **2021**, *50*, 303–328. [CrossRef]
10. Horst, D.D.J.; Duvoisin, D.C.A.; de Almeida Vieira, D.R. Additive Manufacturing at Industry 4.0: A Review. *Int. J. Eng. Tech. Res.* **2018**, *8*, 3–8.
11. Briard, T.; Segonds, F.; Zamariola, N. G-DfAM: A Methodological Proposal of Generative Design for Additive Manufacturing in the Automotive Industry. *Int. J. Interact. Des. Manuf.* **2020**, *14*, 875–886. [CrossRef]
12. Ntintakis, I.; Stavroulakis, G.E.; Sfakianakis, G.; Fiotodimitrakis, N. Utilizing Generative Design for Additive Manufacturing. In *Recent Processes and Manufacturing Advances in Systems Select Proceedings of RAM 2021*; Dave, H.K., Dixit, U.S., Nedelcu, D., Eds.; Springer Nature: Singapore, 2021; ISBN 978-981-16-7786-1.
13. *Martin Leary Design For Additive Manufactruing*; Elsevier: Amsterdam, The Netherlands, 2020; ISBN 0128168870/9780128168875.
14. Taufek, T.; Adenan, M.S.; Manurung, Y.H.P.; Sulaiman, S.A.; Zaid, N.S.; Romzi, N.A.S. 3D Metal Printing Using Generative Design and Numerical Computation. In *Recent Trends in Manufacturing and Materials Towards Industry 4.0*; Springer Nature: Singapore, 2021; pp. 839–849. ISBN 9789811595042.
15. Junk, S.; Rothe, N. Lightweight Design of Automotive Components Using Generative Design with Fiber-Reinforced Additive Manufacturing. *Procedia CIRP* **2022**, *109*, 119–124. [CrossRef]
16. Formlabs 3D Printing Technology Comparison: FDM vs. SLA vs. SLS. Available online: https://formlabs.com/blog/fdm-vs-sla-vs-sls-how-to-choose-the-right-3d-printing-technology/ (accessed on 4 July 2023).
17. Chae, M.P.; Rozen, W.M.; McMenamin, P.G.; Findlay, M.W.; Spychal, R.T.; Hunter-Smith, D.J. Emerging Applications of Bedside 3D Printing in Plastic Surgery. *Front. Surg.* **2015**, *2*, 25. [CrossRef]
18. Dawoud, M.; Taha, I.; Ebeid, S.J. Mechanical Behaviour of ABS: An Experimental Study Using FDM and Injection Moulding Techniques. *J. Manuf. Process.* **2016**, *21*, 39–45. [CrossRef]
19. Lay, M.; Thajudin, N.L.N.; Hamid, Z.A.A.; Rusli, A.; Abdullah, M.K.; Shuib, R.K. Comparison of Physical and Mechanical Properties of PLA, ABS and Nylon 6 Fabricated Using Fused Deposition Modeling and Injection Molding. *Compos. Part B Eng.* **2019**, *176*, 107341. [CrossRef]
20. Vieyra, H.; Molina-Romero, J.M.; Calderón-Nájera, J.d.D.; Santana-Díaz, A. Engineering, Recyclable, and Biodegradable Plastics in the Automotive Industry: A Review. *Polymers* **2022**, *14*, 3412. [CrossRef]
21. Patil, A.; Patel, A.; Purohit, R. An Overview of Polymeric Materials for Automotive Applications. *Mater. Today Proc.* **2017**, *4*, 3807–3815. [CrossRef]
22. Grand View Research. Automotive Plastics Market Size & Share Report, 2030 ID: 978-1-68038-193-1. Available online: https://www.grandviewresearch.com/industry-analysis/automotive-plastics-market (accessed on 8 June 2023).
23. Market Research Report by Fortune Business Insights. Nylon Market Size by Type, by Application and Regional Forecast, 2020–2027. 2020. Available online: https://www.fortunebusinessinsights.com/nylon-market-102007 (accessed on 4 July 2023).
24. Fiore, V.; Scalici, T.; Di Bella, G.; Valenza, A. A Review on Basalt Fibre and Its Composites. *Compos. Part B Eng.* **2015**, *74*, 74–94. [CrossRef]
25. Shanmugam, V.; Rajendran, D.J.J.; Babu, K.; Rajendran, S.; Veerasimman, A.; Marimuthu, U.; Singh, S.; Das, O.; Neisiany, R.E.; Hedenqvist, M.S.; et al. The Mechanical Testing and Performance Analysis of Polymer-Fibre Composites Prepared through the Additive Manufacturing. *Polym. Test.* **2021**, *93*, 106925. [CrossRef]
26. Arockiam, A.J.; Subramanian, K.; Padmanabhan, R.G.; Selvaraj, R.; Bagal, D.K.; Rajesh, S. A Review on PLA with Different Fillers Used as a Filament in 3D Printing. *Mater. Today Proc.* **2022**, *50*, 2057–2064. [CrossRef]
27. Ghabezi, P.; Flanagan, T.; Harrison, N. Short Basalt Fibre Reinforced Recycled Polypropylene Filaments for 3D Printing. *Mater. Lett.* **2022**, *326*, 132942. [CrossRef]

28. Zhang, H.; Sun, W. fu Mechanical Properties and Failure Behavior of 3D Printed Thermoplastic Composites Using Continuous Basalt Fiber under High-Volume Fraction. *Def. Technol.* 2022, *in press*. [CrossRef]
29. Blaine, R.L. *Thermal Applications Note Polymer Heats of Fusion*; TA Instruments: New Castle, DE, USA; Volume TN048.
30. Cardona, C.; Curdes, A.H.; Isaacs, A.J. Effects of Filament Diameter Tolerances in Fused Filament Fabrication. *IU J. Undergrad. Res.* **2016**, *2*, 44–47. [CrossRef]
31. Esmizadeh, E.; Tzoganakis, C.; Mekonnen, T.H. Degradation Behavior of Polypropylene during Reprocessing and Its Biocomposites: Thermal and Oxidative Degradation Kinetics. *Polymers* **2020**, *12*, 1627. [CrossRef]
32. Touris, A.; Turcios, A.; Mintz, E.; Pulugurtha, S.R.; Thor, P.; Jolly, M.; Jalgaonkar, U. Effect of Molecular Weight and Hydration on the Tensile Properties of Polyamide 12. *Results Mater.* **2020**, *8*, 100149. [CrossRef]
33. Starkweather, H.W. The Sorption of Water by Nylons. *J. Appl. Polym. Sci.* **1959**, *2*, 129–133. [CrossRef]
34. Jose, S.; Thomas, S.; Biju, P.K.; Koshy, P.; Karger-Kocsis, J. Thermal Degradation and Crystallisation Studies of Reactively Compatibilised Polymer Blends. *Polym. Degrad. Stab.* **2008**, *93*, 1176–1187. [CrossRef]
35. Chiu, F.C.; Chu, P.H. Characterization of Solution-Mixed Polypropylene/Clay Nanocomposites without Compatibilizers. *J. Polym. Res.* **2006**, *13*, 73–78. [CrossRef]
36. Franciszczak, P.; Wojnowski, J.; Kalniņš, K.; Piesowicz, E. The Influence of Matrix Crystallinity on the Mechanical Performance of Short-Fibre Composites–Based on Homo-Polypropylene and a Random Polypropylene Copolymer Reinforced with Man-Made Cellulose and Glass Fibres. *Compos. Part B Eng.* **2019**, *166*, 516–526. [CrossRef]
37. Ma, N.; Liu, W.; Ma, L.; He, S.; Liu, H.; Zhang, Z.; Sun, A.; Huang, M.; Zhu, C. Crystal Transition and Thermal Behavior of Nylon 12. *E-Polymers* **2020**, *20*, 346–352. [CrossRef]
38. Mao, B.; Cebe, P. Avrami Analysis of Melt Crystallization Behavior of Trogamid. *J. Therm. Anal. Calorim.* **2013**, *113*, 545–550. [CrossRef]
39. Bahrami, M.; Lavayen-Farfan, D.; Martínez, M.A.; Abenojar, J. Experimental and Numerical Studies of Polyamide 11 and 12 Surfaces Modified by Atmospheric Pressure Plasma Treatment. *Surf. Interfaces* **2022**, *32*, 102154. [CrossRef]
40. Acierno, S.; Van Puyvelde, P. Rheological Behavior of Polyamide 11 with Varying Initial Moisture Content. *J. Appl. Polym. Sci.* **2005**, *97*, 666–670. [CrossRef]
41. Filippone, G.; Carroccio, S.C.; Mendichi, R.; Gioiella, L.; Dintcheva, N.T.; Gambarotti, C. Time-Resolved Rheology as a Tool to Monitor the Progress of Polymer Degradation in the Melt State-Part I: Thermal and Thermo-Oxidative Degradation of Polyamide 11. *Polymer* **2015**, *72*, 134–141. [CrossRef]
42. Sergi, C.; Vitiello, L.; Dang, P.; Russo, P.; Tirillò, J.; Sarasini, F. Low Molecular Weight Bio-Polyamide 11 Composites Reinforced with Flax and Intraply Flax/Basalt Hybrid Fabrics for Eco-Friendlier Transportation Components. *Polymers* **2022**, *14*, 5053. [CrossRef]
43. Sodeifian, G.; Ghaseminejad, S.; Yousefi, A.A. Preparation of Polypropylene/Short Glass Fiber Composite as Fused Deposition Modeling (FDM) Filament. *Results Phys.* **2019**, *12*, 205–222. [CrossRef]
44. Milosevic, M.; Stoof, D.; Pickering, K.L. Characterizing the Mechanical Properties of Fused Deposition Modelling Natural Fiber Recycled Polypropylene Composites. *J. Compos. Sci.* **2017**, *1*, 7. [CrossRef]
45. Milovanović, A.; Golubović, Z.; Babinský, T.; Šulák, I.; Mitrović, A. Tensile Properties of Polypropylene Additively Manufactured By FDM. *Struct. Integr. Life* **2022**, *22*, 305–308.
46. Carneiro, O.S.; Silva, A.F.; Gomes, R. Fused Deposition Modeling with Polypropylene. *Mater. Des.* **2015**, *83*, 768–776. [CrossRef]
47. Jin, M.; Giesa, R.; Neuber, C.; Schmidt, H.W. Filament Materials Screening for FDM 3D Printing by Means of Injection-Molded Short Rods. *Macromol. Mater. Eng.* **2018**, *303*, 1800507. [CrossRef]
48. Sergi, C.; Tirillò, J.; Iacovacci, C.; Sarasini, F. Influence of Reprocessing Cycles on the Morphological, Thermal and Mechanical Properties of Flax / Basalt Hybrid Polypropylene Composites. *Sustain. Mater. Technol.* **2023**, *36*, e00648. [CrossRef]
49. Karmaker, A.C.; Youngquist, J.A. Injection Molding of Polypropylene Reinforced with Short Jute Fibers. *J. Appl. Polym. Sci.* **1996**, *62*, 1147–1151. [CrossRef]
50. Farotti, E.; Natalini, M. Injection Molding. Influence of Process Parameters on Mechanical Properties of Polypropylene Polymer. A First Study. *Procedia Struct. Integr.* **2018**, *8*, 256–264. [CrossRef]
51. Yu, S.; Oh, K.H.; Hong, S.H. Enhancement of the Mechanical Properties of Basalt Fiber-Reinforced Polyamide 6,6 Composites by Improving Interfacial Bonding Strength through Plasma-Polymerization. *Compos. Sci. Technol.* **2019**, *182*, 107756. [CrossRef]
52. Sergi, C.; Sbardella, F.; Lilli, M.; Tirillò, J.; Calzolari, A.; Sarasini, F. Hybrid Cellulose–Basalt Polypropylene Composites with Enhanced Compatibility: The Role of Coupling Agent. *Molecules* **2020**, *25*, 4384. [CrossRef]
53. Liu, H.; Yu, Y.; Liu, Y.; Zhang, M.; Li, L.; Ma, L.; Sun, Y.; Wang, W. A Review on Basalt Fiber Composites and Their Applications in Clean Energy Sector and Power Grids. *Polymers* **2022**, *14*, 2376. [CrossRef]
54. Ferreira, I.; Melo, C.; Neto, R.; Machado, M.; Alves, J.L.; Mould, S. Study of the Annealing Influence on the Mechanical Performance of PA12 and PA12 Fibre Reinforced FFF Printed Specimens. *Rapid Prototyp. J.* **2020**, *26*, 1761–1770. [CrossRef]
55. Liao, G.; Li, Z.; Cheng, Y.; Xu, D.; Zhu, D.; Jiang, S.; Guo, J.; Chen, X.; Xu, G.; Zhu, Y. Properties of Oriented Carbon Fiber/Polyamide 12 Composite Parts Fabricated by Fused Deposition Modeling. *Mater. Des.* **2018**, *139*, 283–292. [CrossRef]
56. Feng, L.; Wang, Y.; Wei, Q. PA12 Powder Recycled from SLS for FDM. *Polymers* **2019**, *11*, 727. [CrossRef]

57. Meyer, T.; Harland, A.; Haworth, B.; Holmes, C.; Lucas, T.; Sherratt, P. The Influence of Different Melt Temperatures on the Mechanical Properties of Injection Molded PA-12 and the Post Process Detection by Thermal Analysis. *Int. Polym. Process.* **2017**, *32*, 90–101. [CrossRef]
58. Nicharat, A.; Sapkota, J.; Weder, C.; Johan Foster, E. Melt Processing of Polyamide 12 and Cellulose Nanocrystals Nanocomposites. *J. Appl. Polym. Sci.* **2015**, *132*, 1–10. [CrossRef]